ELSEVIER

Available online at www.sciencedirect.com
SCIENCE DIRECT®

Coastal Engineering xx (2004) xxx–xxx

Coastal Engineering
An International Journal for Coastal, Harbour and Offshore Engineers

www.elsevier.com/locate/coastaleng

Vertical flow structure during Sandy Duck: observations and modeling ☆

A.J.H.M. Reniers[a,*], E.B. Thornton[b], T. Stanton[b], J.A. Roelvink[c]

[a] Department of Civil Engineering and Geosciences, Delft University of Technology, Postbus 5048, 2600 GA, Delft, The Netherlands
[b] Oceanography Department, Naval Postgraduate School, Monterey, CA, USA
[c] WL-Delft Hydraulics and Delft University of Technology, Delft, The Netherlands

Received 10 September 2003; received in revised form 15 January 2004; accepted 6 February 2004

Abstract

Observations of the vertical distribution of time-averaged cross-shore and alongshore flows during the Sandy Duck field experiment are compared with model predictions to assess the parameters governing the flow behaviour. The measurements were obtained with a vertical stack of eight two-component current meters, with the lowest and highest sensor at, respectively O(0.1) and O(2.7) m, above the bed. Observations under breaking wave conditions within the surfzone show that the maximum return flow velocities occur in the lower part of the water column, consistent with laboratory observations. Under non-breaking conditions outside the surfzone the maximum return flow velocities are observed closer to the water surface, again in line with laboratory results. Analogous to previous observations the measured longshore current velocity profiles are logarithmic under non-breaking conditions and become more depth-uniform under breaking conditions. The model description of the vertical structure of the flow includes the presence of wind stresses, wave stresses, pressure gradients, turbulent eddy viscosity and a wave boundary layer. The model utilizes parabolic shape functions to describe the vertical distribution of the turbulent eddy viscosity in the middle layer and within the bottom boundary layer. Eddy viscosity is enhanced in regions where turbulence is produced, i.e. near the surface in the case of breaking waves and within the bottom boundary layer. Estimates of the wave-breaking-induced turbulent eddy viscosity and bottom friction are obtained by minimizing the model–measurement discrepancies. Predictions utilizing calibrated expressions for both the turbulent eddy viscosity and bottom friction are in general agreement with the observations, provided the wave transformation and associated mass flux are modeled correctly and a parabolic eddy viscosity distribution is used. Using a piecewise constant eddy viscosity distribution generally results in a degrading of the agreement between measurements and model results.

Keywords: Longshore currents; Return flow; Vertical velocity profiles; Field measurements; Modeling

1. Introduction

Nearshore cross-shore flows can exhibit strong curvature in the vertical associated with the vertical imbalance between the wave forcing and cross-shore pressure gradients acting on the water column (Dyhr-

☆ This manuscript was prepared with AGU's Latex macros v5, with the extension package 'AGU^{++}' by P.W. Daly, version 1.6b from 1999/08/19.

* Corresponding author. Tel.: +31-15-278-4778; fax: +31-15-278-4248.

E-mail address: ad@dutcvmm.ct.tudelft.nl (A.J.H.M. Reniers).

0378-3839/$ - see front matter
doi:10.1016/j.coastaleng.2004.02.001

Nielsen and Sorensen, 1970). This strong curvature has been observed under laboratory conditions (Stive and Wind, 1986; Hansen and Svendsen, 1984; Okayasu et al., 1988; Arcilla et al., 1994; Ting and Kirby, 1994) and during field conditions (Smith et al., 1992; Haines and Sallenger, 1994; Garcez Faria et al., 2000). Differences between the curvature obtained under laboratory and field conditions have been observed. Laboratory measurements typically show the strongest velocities in the return flow close to the bed. Haines and Sallenger (1994) observed maximum flow velocities closer to the middle of the water column, and they concluded that eddy viscosity models based on laboratory experiments would therefore not be warranted for the interpretation of (their) field measurements. Garcez Faria et al. (2000) observed vertical distributions that were more like the laboratory observations. Still, in all the field experiment cases, the resolution close to the bed was limited, preventing firm conclusions with respect to the apparent differences between laboratory and field conditions. The vertical profile field measurements presented here do resolve the lower part of the water column.

The curvature of the cross-shore flow is a function of wave forcing, set-up gradients, turbulent eddy viscosity, bottom roughness and wind. Under breaking waves, the cross-shore flow generally exhibits a strong shear close to the surface associated with the shear stress exerted on the water column by the breaking waves (Stive and Wind, 1986). A similar effect is associated with the wind stress at the water surface, though the wave stresses in breaking waves typically exceed the wind stress by an order of magnitude (Whitford and Thornton, 1993), and the resulting velocity shear is expected to be less prominent. Near the bed, boundary layer effects become important with an enhanced eddy viscosity close to the bed associated with the dissipation of wave energy through bottom friction, and an onshore directed driving force within the bottom boundary layer. In the absence of wave breaking, this results in an onshore flow, or streaming, close to the bed (Longuet-Higgins, 1953). Once wave breaking becomes important, the resulting set-up gradient within the surfzone dominates the force balance in the bottom boundary layer, resulting in an offshore directed flow close to the bed (e.g. Haines and Sallenger, 1994).

Longshore current velocity distributions typically show less curvature outside the wave boundary layer and correspond closely to logarithmic profiles in both laboratory (Visser, 1984; Simons et al., 1992; Hamilton and Ebersole, 2001) and field conditions (Garcez Faria et al., 1998), given the fact that there is no vertical imbalance in the forcing. Based on observations by Visser (1984), Svendsen and Lorenz (1989) suggested that in the presence of strong wave breaking the observed velocity profile may become more depth-uniform, as the wave breaking-induced turbulence introduces strongly enhanced mixing (Church and Thornton, 1993). This was confirmed by the observations of Garcez Faria et al. (2000). Additional effects are caused by the small-scale bed topography, which can vary significantly throughout the nearshore (Thornton et al., 1998, Gallagher et al., 2003), thus contributing to the deviations from the expected logarithmic velocity distribution.

Mean flow distributions in the alongshore and cross-shore direction are often examined separately, using different descriptions for the vertical distribution of the turbulent eddy viscosity. Under breaking waves, the eddy viscosity within the bottom boundary layer is typically smaller than in the middle layer (Nadaoka and Kondoh, 1982). However, in the absence of wave breaking, the turbulent eddy viscosity in the bottom boundary layer exceeds the eddy viscosity in the middle layer (Jonsson, 1966). To account for the differences in turbulent eddy viscosity, most models discriminate between three layers, the surface-trough layer which encompasses the wave troughs and crests, the middle layer and the bottom boundary layer. The vertical distribution of the eddy viscosity utilized in the modeling of the return flow ranges from depth-invariant (Svendsen, 1984; Stive and Wind, 1986; Van Dongeren and Svendsen, 2000), linear with depth (Okayasu et al., 1988), quadratic (Garcez Faria et al., 2000), parabolic (Roelvink and Reniers, 1994), and exponential (Svendsen, 1984). The vertical eddy viscosity distribution in solving for the longshore current profile is generally assumed to be parabolic (Garcez Faria et al., 1998), resulting in logarithmic velocity profiles, or depth-invariant (Svendsen and Lorenz, 1989), resulting in parabolic velocity profiles. The effects of linearly and quadratically varying turbulent eddy viscosity distributions on the longshore current velocity profiles were examined by Dong and

Anatasiou (1991). There is no apparent physical reason why the vertical distribution of the eddy viscosity should be anisotropic in the vertical plane. Hence, it is plausible and more consistent to utilize a single description of the eddy viscosity distribution in the vertical for both cross-shore and alongshore flows (de Vriend and Stive, 1987; Svendsen and Lorenz, 1989; Van Dongeren and Svendsen, 2000).

Another important difference in modeling of the return flow is the definition of the boundary conditions. All models are constrained by the mass-flux condition in which the depth-integrated return flow has to equal the wave-induced mass-flux. The second boundary condition is imposed either as the streaming velocity at the top of the wave-boundary layer (Dally, 1980; Svendsen, 1984), a shear stress at the surface (Stive and Wind, 1986; Garcez Faria et al., 2000), a near-bed velocity (Svendsen et al., 1987), or a no-slip condition at the bed (Svendsen and Buhr Hansen, 1988, Haines and Sallenger, 1989).

In the following, the model by Roelvink and Reniers (1994) (denoted RR94 hereafter) is utilized to describe the curvature of cross-shore and alongshore flow as a function of the various forcing mechanisms in combination with a parabolic distribution for the turbulent eddy viscosity. Eddy viscosity is enhanced in regions where turbulence is produced, i.e. near the surface in the case of breaking waves and within the bottom boundary layer. The model utilizes parabolic shape functions (Davies, 1988) to describe the vertical distribution in both the middle layer and the bottom boundary layer, resulting in logarithmic solutions for the vertical distribution of the flow field. A shear stress condition is applied at the trough level combined with a no-slip condition at the bottom. The mass-flux constraint is used to determine the depth-invariant forcing that is not known a priori (described below).

The overall objective of this study is to examine the sensitivity of model output to the input of turbulent eddy viscosity and bottom friction parameters, and to calibrate these parameters so that the model can be used in a predictive sense. To that end, differences between model predictions and measurements of the vertical flow structure obtained during the Sandy Duck field experiment are minimized. The focus is on near-bed velocities, which are important in sediment transport modeling.

Only a brief description of the velocity profile model is given in RR94. Here a detailed description of the model formulations and assumptions is given in Section 2. The field measurements obtained during the Sandy Duck field experiment are described in Section 3. Model measurement data comparisons (Section 4) are followed by a discussion and conclusions.

2. Model description

The model of RR94 is used to predict the vertical distribution of the cross-shore flow. The model is based on the concepts formulated by de Vriend and Stive (1987), defining a top layer above trough level, a middle layer and a bottom boundary layer. In the following, all quantities are assumed to be averaged over many wave periods of a stationary wave field thus representing mean conditions. The time-averaged momentum balance for the middle layer is given by:

$$\frac{\partial \tau_i}{\partial \sigma} = F_i \tag{1}$$

where the subscript denotes either the cross-shore direction x (positive onshore) or alongshore direction y, τ_i is the shear stress, F_i the depth-invariant forcing per unit volume within the middle layer and σ represents the non-dimensional vertical position positive upward from the bed:

$$\sigma = \frac{h_{\rm t} + z}{h_{\rm t}} \tag{2}$$

where z is positive upward from the trough level, $h_{\rm t}$, which is given by:

$$h_{\rm t} = h - \frac{H_{m0}}{2} \tag{3}$$

where h represents the mean water depth (including set-up) and H_{m0} the significant wave height. The shear stress distribution within the middle layer can be obtained by integrating Eq. (1) along the σ-axis:

$$\tau_i = \tau_{{\rm t},i} - F_i(1 - \sigma) \tag{4}$$

where $\tau_{{\rm t},i}$ represents the shear stress at the trough level, denoted by subscript t, and is the sum of shear stresses associated with the presence of breaking waves (Stive and Wind, 1986) and wind. The wave breaking related shear stress at the trough level is given by (Deigaard, 1993):

$$\tau_{\mathrm{wave},i} = \frac{D_{\mathrm{r}} k_i}{\omega} \tag{5}$$

analogous to the driving of nearshore currents (Dingemans et al., 1987), where D_{r} is the dissipation of roller energy, ω is the peak radial frequency of the short waves and k_i the wave number component at the peak frequency. It is assumed that the total rotational wave forcing can be applied as a stress at the trough level. The wind stress, $\tau_{\mathrm{wind},i}$, is given by:

$$\tau_{\mathrm{wind},i} = c_{\mathrm{d}} \rho_{\mathrm{a}} |W| W_i \tag{6}$$

where $|W|$ is the wind speed, ρ_{a} is the air density and the drag coefficient, c_{d}, is set at 0.002 (Ruessink et al., 2001).

The shear stress is related to the gradient of the mean horizontal velocity through the turbulent eddy viscosity, ν_{t}:

$$\tau_i = \rho \frac{\nu_{\mathrm{t}}}{h} \frac{\partial u_i}{\partial \sigma} \tag{7}$$

where ν_{t} is equated to a product of a shape factor, ϕ_{s}, and a parabolic shape function:

$$\nu_{\mathrm{t}} = \phi_{\mathrm{s}} \bar{\nu}_{\mathrm{t}} \sigma (\sigma_{\mathrm{s}} - \sigma) \tag{8}$$

where $\bar{\nu}_{\mathrm{t}}$ is the depth-averaged turbulent eddy viscosity for the middle layer and σ_{s} represents the upper limit at which the eddy viscosity is zero (Appendix A, Fig. A1). Three potential contributions to the turbulent eddy viscosity are considered; wave-breaking-induced turbulence, wind-induced turbulence and flow-generated turbulence. The wave-breaking-induced, depth-averaged, eddy viscosity is given by (Battjes, 1975):

$$\bar{\nu}_{\mathrm{t,wave}} = f_v H_{\mathrm{rms}} \left(\frac{D_{\mathrm{r}}}{\rho} \right)^{\frac{1}{3}} \tag{9}$$

where a calibration factor f_v has been added and H_{rms} represents the root mean square wave height. The depth-averaged wind-generated eddy viscosity is given by:

$$\bar{\nu}_{\mathrm{t,wind}} = \frac{1}{3} \kappa h_{\mathrm{t}} \sqrt{\frac{|\tau_{\mathrm{wind}}|}{\rho}} \tag{10}$$

where κ is von Kármán's constant. The depth-averaged flow induced eddy viscosity:

$$\bar{\nu}_{\mathrm{t,flow}} = \frac{1}{6} \kappa h_{\mathrm{t}} \sqrt{g h_{\mathrm{t}} \left| \frac{\partial \bar{\eta}}{\partial y} \right|} \tag{11}$$

with $\bar{\eta}$ the mean water level and g the gravitational acceleration. In the presence of combined waves, wind and flow the eddy viscosities are summed together in an heuristic way to obtain the total depth-averaged turbulent eddy viscosity:

$$\bar{\nu}_{\mathrm{t}} = \sqrt{\bar{\nu}^2_{\mathrm{t,flow}} + \bar{\nu}^2_{\mathrm{t,wind}} + \bar{\nu}^2_{\mathrm{t,wave}}} \tag{12}$$

assuming the eddy viscosity squared is a measure of turbulent kinetic energy instead of a straightforward summation of the individual eddy viscosity contributions as suggested by de Vriend and Stive (1987).

In the case of a purely slope-driven current, the eddy viscosity is assumed to be zero at the bed and at the water surface, i.e. $\sigma_{\mathrm{s}} = 1$. In the case of a purely wave-driven or wind-driven flow the eddy viscosity is assumed to be zero at the bed and to have a maximum at the water surface, i.e. $\sigma_{\mathrm{s}} = 2$. In the case of a combined slope and wave/wind-driven flow, σ_{s} and ϕ_{s} depend on the magnitude of the individual contributions to the total eddy viscosity (Appendix A).

Using Eqs. (7) and (8), the gradient of the flow velocity within the middle layer is given by:

$$\frac{\partial u_i}{\partial \sigma} = \frac{h_{\mathrm{t}}}{\rho \phi_{\mathrm{s}} \bar{\nu}_{\mathrm{t}}} \left(\frac{\tau_{\mathrm{t},i} - F_i (1 - \sigma)}{\sigma (\sigma_{\mathrm{s}} - \sigma)} \right) \tag{13}$$

which can be solved analytically for u_i, provided F_i is known, and utilizing the velocity at the top of the bottom boundary layer (described below) as a boundary condition (Appendix B, Eq. (B6)).

Within the bottom boundary layer, the dissipation of short wave energy due to bottom friction results in a time-averaged shear stress, $\rho < \tilde{u}_i \tilde{w} >$ (Longuet-Higgins, 1953), where w is the vertical velocity, the tilde indicates short wave quantities and $<>$ denotes ensemble averaging. This shear stress is zero at the bed and reaches an asymptotic value at the top of the wave boundary:

$$\rho \frac{\partial < \tilde{u}_i \tilde{w} >}{\partial \sigma} = -\frac{1}{\delta} \frac{D_{\mathrm{f}} k_i}{\omega} \tag{14}$$

where D_{f} represents the dissipation of wave energy due to bottom friction and δ is the thickness of the bottom boundary layer scaled with the local water depth (Fredsoe and Deigaard, 1992):

$$\delta = f_{\delta} 0.09 \left(\frac{A}{k_s}\right)^{0.82} \frac{k_s}{h_{\mathrm{t}}} \tag{15}$$

to which a multiplication factor f_{δ} has been added, and A is the near-bed orbital excursion of the short waves associated with the root mean square wave height at the peak frequency. The maximum δ is 0.5 and the minimum δ equals $f_{\delta} \frac{e_{z_0}}{h_{\mathrm{t}}}$, where the zero level, z_0, is given by:

$$z_0 = \frac{k_s}{33} \tag{16}$$

with k_s the Nikuradse roughness. Below $(e_{z_0})/(h_{\mathrm{t}})$ the velocity decreases linearly to a zero value at the bed. Utilizing a f_{δ} of 1 results in the theoretical boundary layer thickness associated with monochromatic waves. Laboratory measurements of the bottom boundary layer under random waves suggest a significant increase in the thickness (Klopman, 1994) with respect to monochromatic wave conditions. In the following f_{δ} is fixed at 3 given the fact that a proper validation requires more detailed measurements close to the bed.

Taking into account the additional forcing within the bottom boundary layer, the vertical momentum balance is given by:

$$\tau_i = \tau_{\mathrm{t},i} - F_i(1-\sigma) + \frac{D_{\mathrm{f}} k_i}{\omega} \frac{(\delta - \sigma)}{\delta} \tag{17}$$

The dissipation due to bottom friction is given by:

$$D_{\mathrm{f}} = \frac{1}{2\sqrt{\pi}} \rho f_{\mathrm{w}} u_{\mathrm{orb}}^3 \tag{18}$$

where u_{orb} represents the near-bed orbital velocity associated with the root mean square wave height at the peak frequency and the friction factor f_{w} is given by (Soulsby, 1997):

$$f_{\mathrm{w}} = 1.39 \left(\frac{A}{z_0}\right)^{-0.52} \tag{19}$$

The turbulent eddy viscosity within the bottom boundary layer is locally enhanced to account for the production of turbulence due to short-wave dissipation associated with bottom roughness:

$$\begin{aligned} \nu_{\mathrm{t}} &= \phi_{\mathrm{s}} \bar{\nu}_{\mathrm{t}} \sigma(\sigma_{\mathrm{s}} - \sigma) + \phi_{\mathrm{b}} \bar{\nu}_{\mathrm{tb}} \sigma(\delta - \sigma) \\ &= (\phi_{\mathrm{s}} \bar{\nu}_{\mathrm{t}} + \phi_{\mathrm{b}} \bar{\nu}_{\mathrm{tb}})(\sigma_{\mathrm{b}} - \sigma)\sigma \end{aligned} \tag{20}$$

where subscripts b refer to the bottom boundary layer and $\bar{\nu}_{\mathrm{tb}}$ represents the additional depth-averaged value of the eddy viscosity:

$$\bar{\nu}_{\mathrm{tb}} = \frac{f_{\mathrm{w}}^2 u_{\mathrm{orb}}^2}{4\omega} \tag{21}$$

The value of σ_{b} and the shape factor ϕ_{b} depend on the relative magnitude of the additional eddy viscosity in the bottom boundary layer and the eddy viscosity distribution in the middle layer (see Appendix A).

Combining Eqs. (7), (17) and (20) to relate the velocity gradient to the shear stresses gives:

$$\frac{\partial u_i}{\partial \sigma} = \frac{h_{\mathrm{t}}}{\rho(\phi_{\mathrm{s}} \bar{\nu}_{\mathrm{t}} + \phi_{\mathrm{b}} \bar{\nu}_{\mathrm{tb}})} \times \left(\frac{(\tau_{\mathrm{t},i} - F_i + \frac{D_{\mathrm{f}} k_i}{\omega}) + (F_i - \frac{D_{\mathrm{f}} k_i}{\delta \omega})\sigma}{\sigma(\sigma_{\mathrm{b}} - \sigma)} \right) \tag{22}$$

Vertical integration of Eq. (22) yields the vertical distribution of the velocity within the bottom boundary layer utilizing a no-slip boundary condition at the bed (Appendix B, Eq. (B12)). Combining Eqs. (B6) and (B12) yields an analytical description of the vertical flow structure within the middle layer and bottom boundary layer that can be compared with measurements.

To solve for the vertical distribution of the flow, a number of local integral wave quantities are required, i.e. depth-invariant forcing (Eq. (4)), roller energy dissipation (Eqs. (5) and (9)), near-bed orbital velocity (Eqs. (18) and (21)), near-bed orbital excursion ((Eqs. (15) and (19)), and the wave number vector (Eqs. (5), (14) and (28)). These integral quantities are generally obtained with a 1D wave propagation model (Haines and Sallenger, 1989, Garcez Faria et al., 2000) or measurements (Svendsen, 1984; Stive and Wind, 1986). To avoid errors in the depth-invariant forcing due to alongshore variation in the bathymetry (Putrevu et al., 1995; Reniers et al., 1995) and shear-instability-

Table 1
Vertical position of the EMF current meters above the bed

Sensor	EMF01	EMF02	EMF03	EMF04	EMF05	EMF06	EMF07	EMF08
z (m)	0.08	0.28	0.53	0.83	1.28	1.75	2.19	2.67

induced mixing (Bowen and Holman, 1989; Ozkan-Haller and Kirby, 1999), neither of which can be obtained from a 1D model, an iterative procedure for F_i is adopted where the double vertical integration of Eqs. (13) and (22) has to equal the measured mass flux in both cross-shore and alongshore directions:

$$\int_0^1 u_{c,i}(\sigma)d\sigma = \frac{1}{z_N}\sum_{j=1}^{j=N}(u_{m,i,j}+u_{m,i,j-1})(z_j - z_{j-1})/2 \tag{23}$$

where the subscripts m and c refer to measured and computed, respectively, subscript j corresponds to the individual sensors (Table 1), $z_0 = 0$ and $u_{m,i,0} = 0$, and z_N corresponds to the position of the uppermost sensor that is still below trough level.

Errors in the wave-forcing (Eq. (5)) associated with alongshore variation in the bathymetry can still be present but are expected to be less important provided the bottom variation is mild (Putrevu et al., 1995). All other integral quantities are obtained from a 1D-wave transformation model described by Reniers and Battjes (1997) (denoted RB97 hereafter) with the wave-breaking dissipation formulation according to Battjes and Janssen (1978), utilizing linear wave theory to relate wave energy to near-bed quantities, such as the orbital velocity and excursion. For a description of the wave transformation model refer to RB97.

The vertical flow model has two tuning parameters that need to be quantified: the bottom roughness k_s,

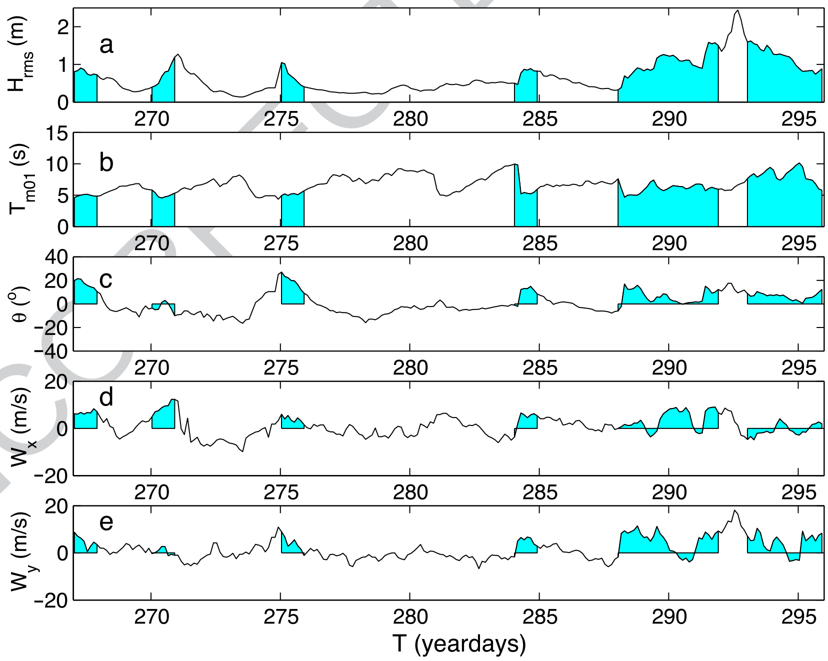

Fig. 1. Climatology during part of the Sandy Duck field experiment. Time periods utilized in model–measurement comparisons indicated by the gray areas.

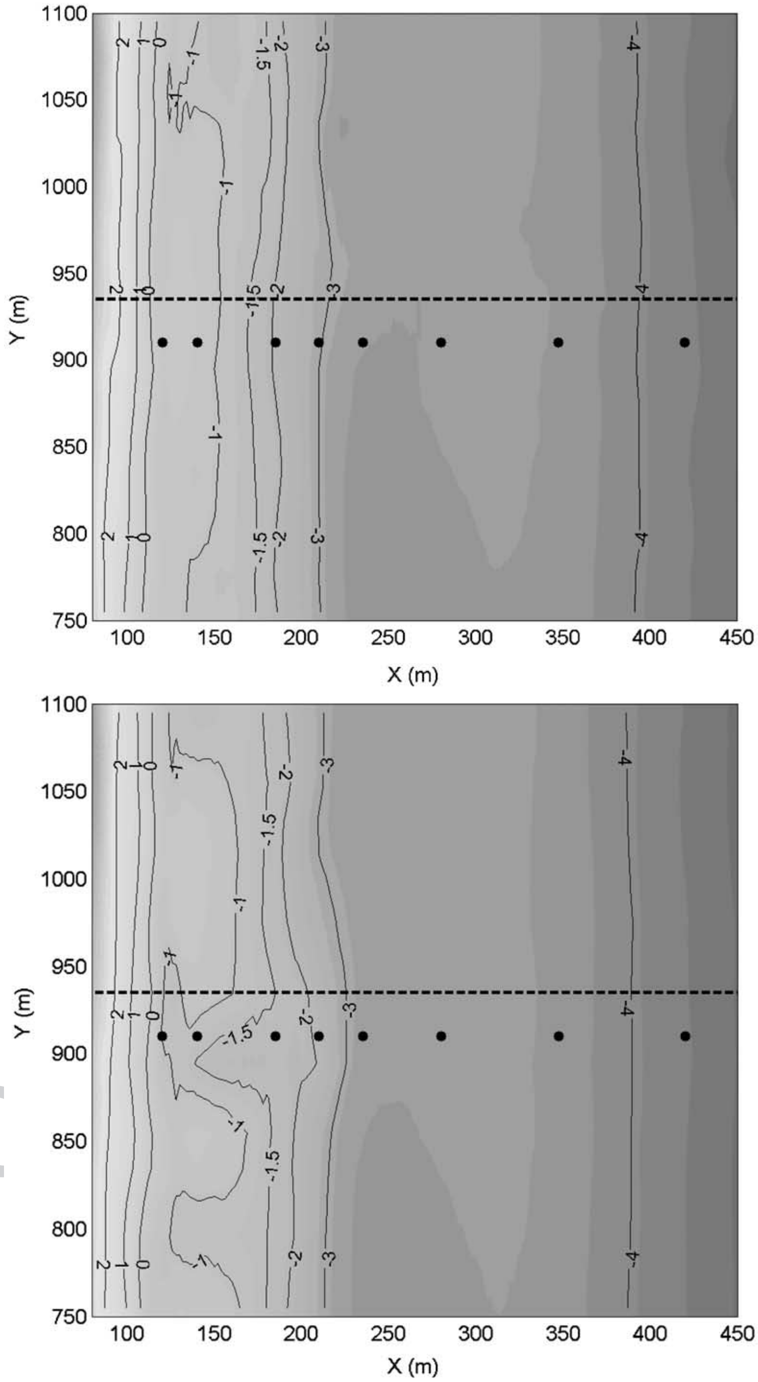

Fig. 2. Bathymetry on yearday 284 (upper panel) and yearday 291 (lower panel) with depth-contours in meters with respect to mean sea level. Pressure sensor locations denoted by dots at $Y = 910$ m. Sled transect indicated by the dashed line at $Y = 935$ m.

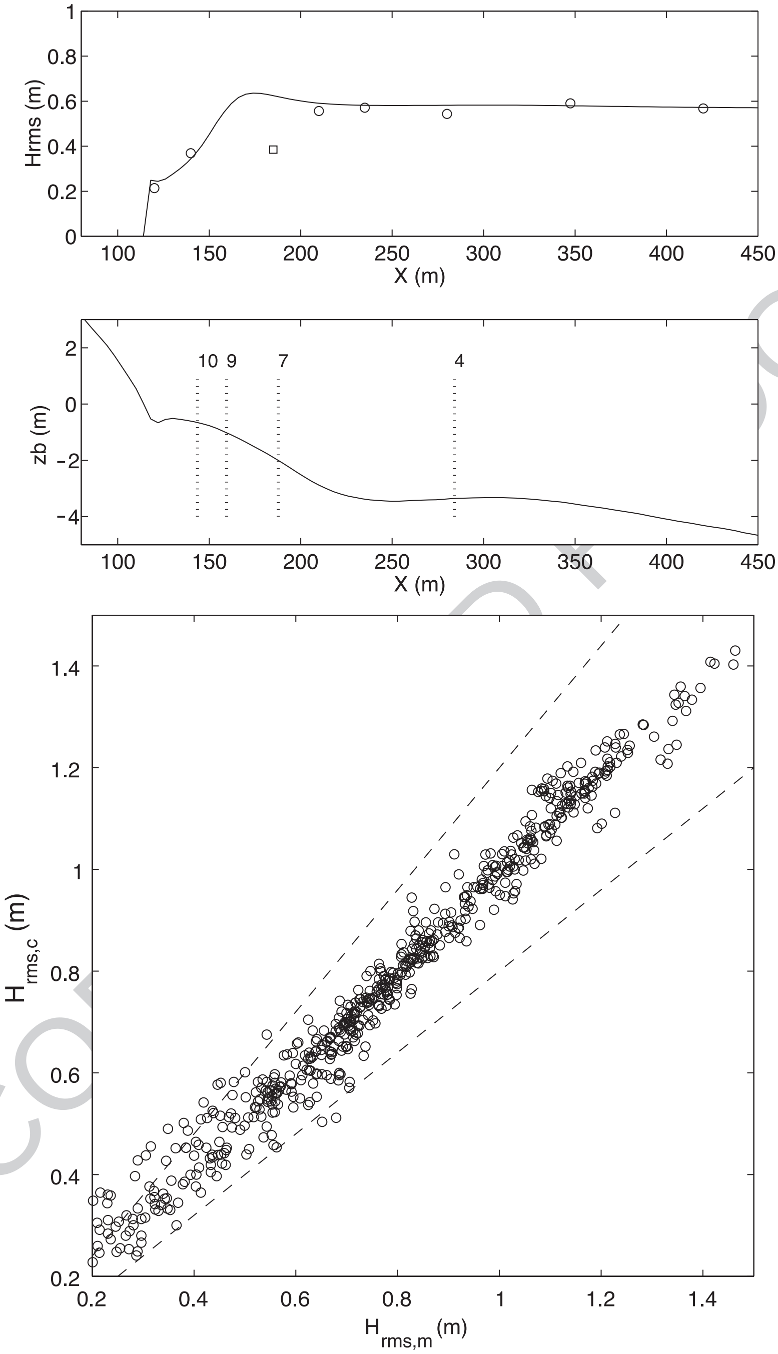

Fig. 3. Upper panel: Example of measured (circles) and computed H_{rms} on yearday 288. Measured H_{rms} at $X=180$ m indicated by square. Middle panel: corresponding cross-shore profile along the pressure array with a number of sled deployment locations discussed below. Lower panel: synopsis of computed and measured H_{rms} at all sensor locations. Results at the sensor located at $X=180$ m have been omitted.

Eq. (16), and the eddy viscosity scale factor f_v, Eq. (9). Comparisons with measurement data will be used to quantify these parameters and examine the model's sensitivity to realistic changes in these parameter values.

3. Sandy Duck experiment

The Sandy Duck experiment was performed in the fall of 1997 at the Field Research Facility (FRF) at Duck (North Carolina), covering a period of approximately 5 weeks. On average, the conditions were mild with offshore root mean square wave heights less than 0.5 m. A modest storm event is centered around yearday 292 (panel a of Fig. 1), during which the incident wave heights briefly exceeded 2 m. Mean wave periods are computed as a first-order moment of the energy density frequency spectrum:

$$T_{m,01} = \frac{\int_{f_l}^{f_h} E(f)df}{\int_{f_l}^{f_h} fE(f)df} \qquad (24)$$

where the low-frequency cut-off, f_l is set at 0.05 Hz and the high frequency cut-off, f_h at 0.3 Hz, range from 5 to 10 s (pnel b of Fig. 1).

Wave directional spectra are measured at the FRF 8 m linear array (Long and Atmadja, 1994) at 3-h intervals based on 2 h and 16 min time series. The mean direction of the incident waves is defined in such a way that the shear component of the radiation

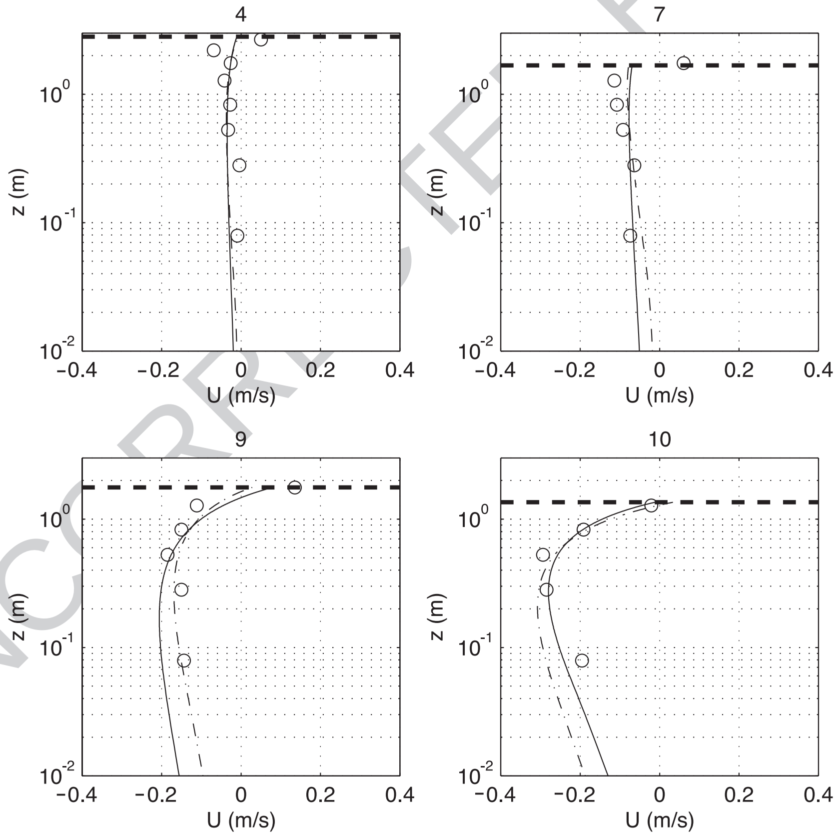

Fig. 4. Examples of the vertical distribution of the cross-shore flow on yearday 288. Measurements obtained with EMF (circles). Computed results for optimized f_v and k_s (solid lines) and calibrated $f_v = 0.101$ m^2/s and bottom roughness $k_s = 0.0082$ m (dashed lines).

stress, computed from the measured frequency directional spectra, is conserved (Thornton and Guza, 1986). Mean wave incidence angles, θ, at the 8 m FRF array were generally small and predominantly from the north with a range of approximately $\pm 20°$ (panel c of Fig. 1).

The wind speed, $|W|$, and direction are measured at the end of the pier at a height of 18.7 m, and have been decomposed into cross-shore W_x and alongshore winds W_y. Cross-shore wind speeds are mostly onshore (i.e. positive) and generally less than 10 m/s. The up or down-coast direction of the alongshore wind velocities coincides in general with the up or down-coast direction (positive and negative W_y, respectively) of the incident waves, consistent with locally generated waves (panel d of Fig. 1).

Data selected for analysis only include times when the offshore wave heights exceeded 0.8 m and measurements are available to ensure a high signal to noise ratio. The selected periods for the comparison contain both mild conditions and moderate storm conditions (see Fig. 1).

The bathymetry offshore of the 2 m depth contour showed little alongshore variability during the experiment. However, closer to shore significant variability could be observed at times (compare panels in Fig. 2). In contrast to earlier experiments at Duck, there was no well-defined inner bar present in the cross-shore profile (Fig. 2).

The vertical profiles of surfzone currents are examined using measurements from a vertical stack of eight electromagnetic flow meters (denoted EMF hereafter) deployed on a mobile sled. The lowest sensor was

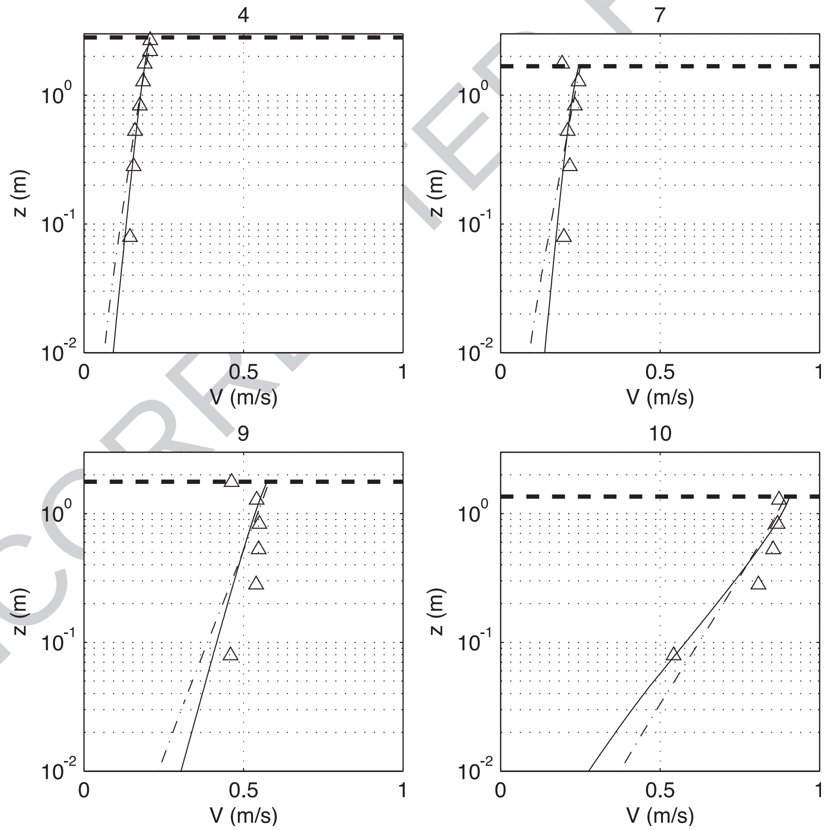

Fig. 5. Examples of the vertical distribution of the alongshore-shore flow on yearday 288. Measurements obtained with EMF (triangles). Computed results for optimized f_v and k_s (solid lines) and calibrated $f_v = 0.101$ m^2/s and bottom roughness $k_s = 0.0082$ m (dashed lines).

located at approximately 8 cm above the bed and the highest sensor at 267 cm (see Table 1 for sensor positions). The actual position of the sensors with respect to the bed depends on the settling of the sled and the presence of bed forms. The sled was deployed along a line north of the FRF pier at $Y = 935$ m (Fig. 2). Early in the morning the Coastal Research Amphibious Buggy (CRAB) towed the sled to a particular position offshore at which the measurements were to be performed for a duration of approximately 1 h. After this period of time, the sled was pulled inshore to a new measurement position, after which another 1 h measurement is performed. Thus by sequentially relocating the sled onshore, a cross-section of the beach was monitored. The sampling frequency for all instruments deployed on the sled was 48 Hz.

In addition to the sled, a cross-shore array of pressure transducers was deployed adjacent to the sled deployment line at $Y = 910$ m (see Fig. 2). Using spectral transfer functions based on linear wave theory to account for the vertical variation of wave dynamics, hourly cross-shore distributions of the surface elevation spectra are obtained. Assuming the wave heights are Rayleigh distributed, the root mean square wave height is obtained by integration of the surface elevation energy density spectrum:

$$H_{\rm rms} = 2\sqrt{2}\sqrt{\int_{f_{\rm l}}^{f_{\rm h}} E_{\eta\eta}(f)df} \tag{25}$$

which is used to calibrate the wave transformation model.

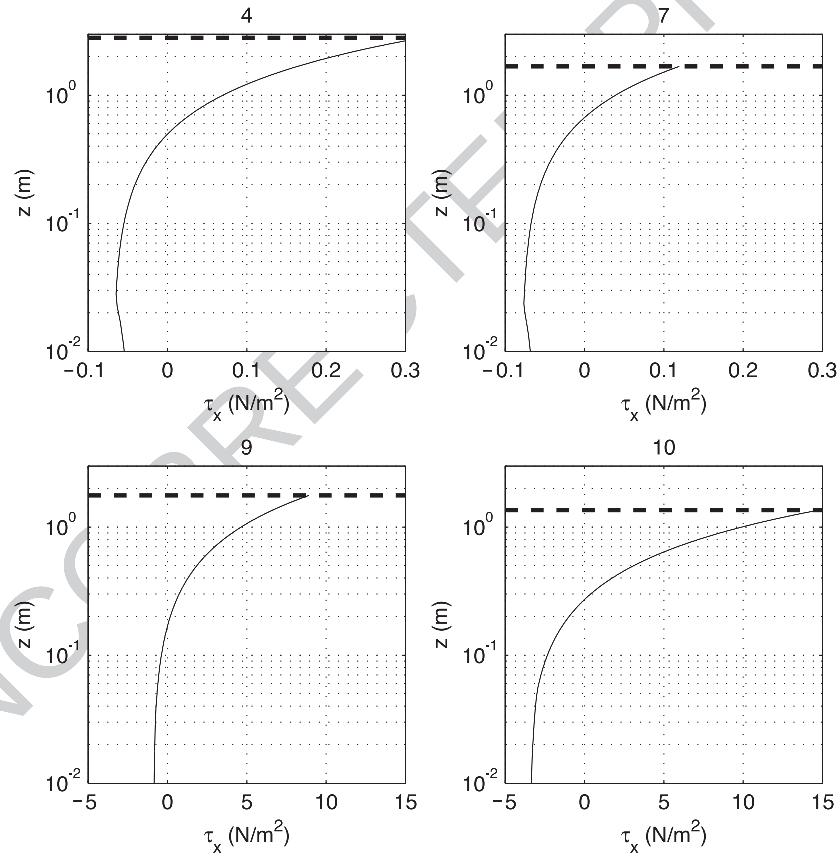

Fig. 6. Examples of the vertical distribution of the cross-shore shear stress on yearday 288 for optimized f_v and k_s. Stations 4 and 7 are outside surfzone, stations 9 and 10 are inside surfzone. Note change of abscissa scale by a factor of 50 between locations outside and inside the surfzone.

4. Comparison with measurements

The integral wave quantities required for the return flow modeling are obtained from the wave transformation model described by RB97. The offshore boundary is imposed at the 8-m depth contour. The sled was repositioned approximately every hour, and the corresponding wave direction at the offshore boundary for a given hour was obtained by linear interpolation of the 3 h FRF mean wave direction data. To avoid errors in the local wave height, i.e. at the sled positions, the wave height measured at the most offshore point of the cross-shore pressure array is inversely shoaled and refracted to the 8 m depth contour.

The wave transformation is optimized for each individual sled measurement position by minimizing the error between the observed $H_{rms,m}$ at the cross-shore pressure array and the computed $H_{rms,c}$ as function of the wave breaking parameter γ (RB97). The pressure sensor located at $X=180$ m showed anomalous behaviour with respect to the other pressure sensors (upper panel of Fig. 3) and has therefore been neglected in the optimization. The optimization of the wave transformation resulted in a mean γ of 0.60 with a standard deviation of 0.15 and errors which are generally within 10% of the measured wave heights (lower panel of Fig. 3), provided the results at $X=180$ are ignored.

Given the integral wave and wind quantities at the sled positions, the vertical flow structure can be computed. The first step is to find the optimal values for both the eddy viscosity scaling factor, f_v, and the bottom roughness, k_s, at each deployment position of

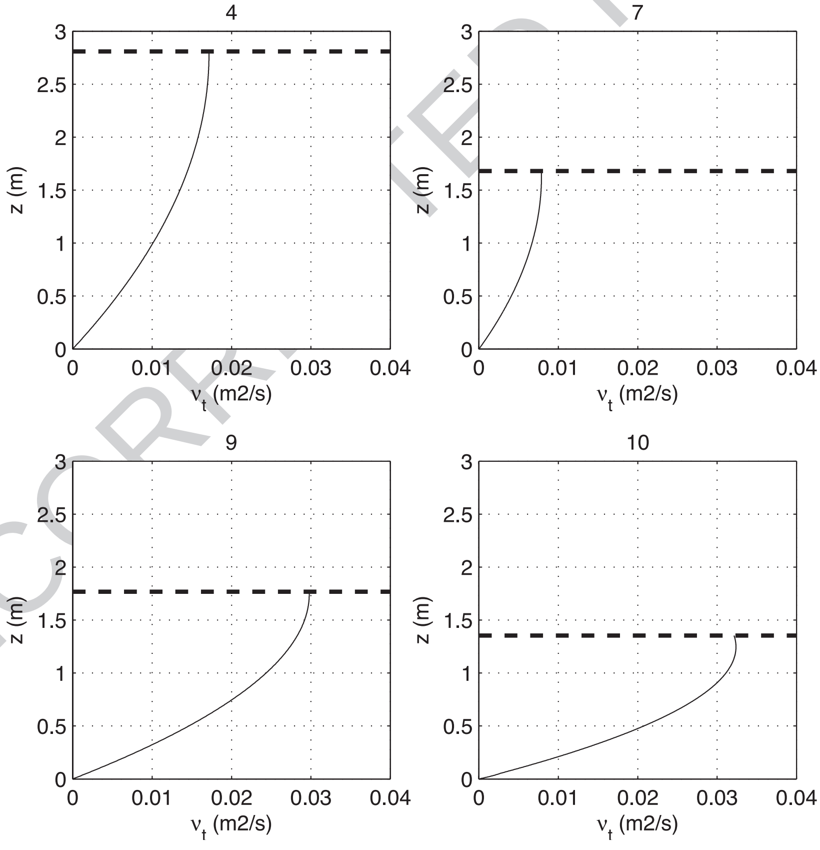

Fig. 7. Examples of the vertical distribution of the turbulent eddy viscosity on yearday 288 for optimized f_v and k_s.

the sled by minimizing the error between measurements and computations. The error is defined as:

$$\epsilon = \sum_{j=1}^{j=N} (u_{\mathrm{m},j} - u_{\mathrm{c},j})^2 + \sum_{j=1}^{j=N} (v_{\mathrm{m},j} - v_{\mathrm{c},j})^2 \tag{26}$$

where the subscript j denotes current meters over the vertical. This approach is similar to Haines and Sallenger (1994) and Garcez Faria et al. (2000); however, here both the cross-shore and alongshore velocity are included in the minimization. The objective is to examine the variation of the optimal values of both the eddy viscosity scale factor and the bottom roughness and obtain representative values that are to be used for the calibrated model predictions.

Typical comparisons of the optimized model predicted and measured vertical flow distribution at locations both outside (4 and 7) and inside (9 and 10) the surfzone (see middle panel of Fig. 3 for locations) show relatively small discrepancies (Figs. 4 and 5). Starting with stations outside the surfzone (4 and 7), measured profiles below the trough level bend slightly backwards (upper panels of Fig. 4), a condition observed earlier by Nadaoka and Kondoh (1982) for non-breaking waves during a laboratory undertow experiment, and examined by Putrevu and Svendsen (1993). As a result, the maximum measured cross-shore flow velocity is near the surface. This behaviour is only partially reproduced by the optimized computational results, given the fact that occasional wave-breaking is present in the model computations. The occasional wave breaking results in an onshore (pos-

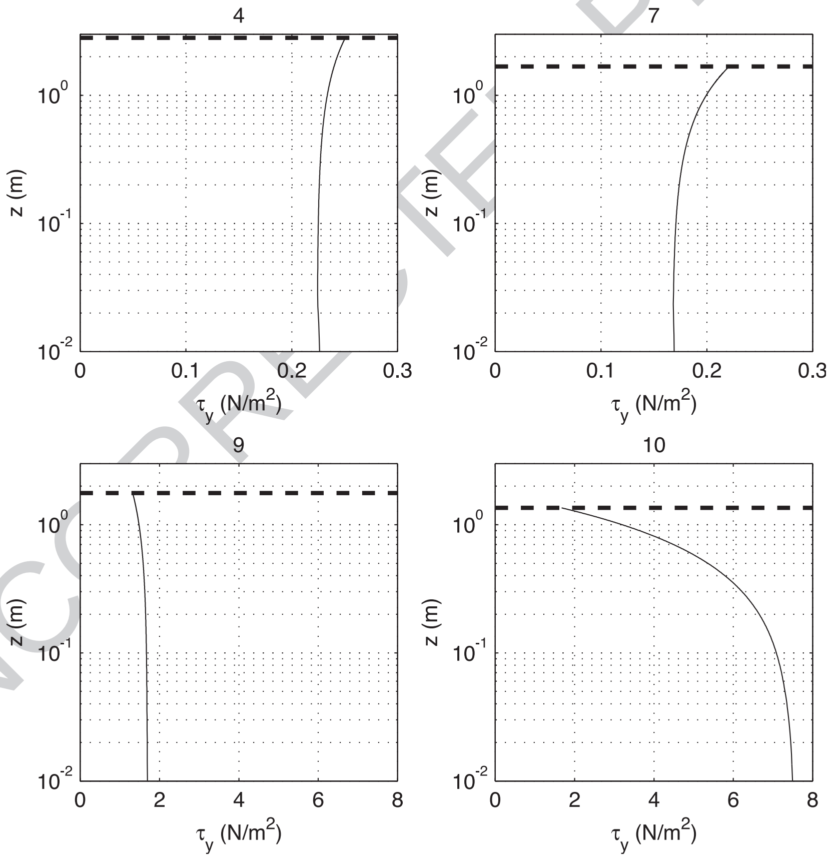

Fig. 8. Examples of the vertical distribution of the alongshore shear stress on yearday 288 for optimized f_v and k_s. Notice the difference in abscissa scales for stations inside (4 and 7) and outside (9 and 10) the surfzone.

itive) directed shear stress at the trough level (upper panels of Fig. 6) and consequently the velocity profiles bend forward near the surface. The degree of forward bending remains limited due to the concomitant increase in the turbulent eddy viscosity at trough level associated with the occasionally breaking waves (see upper panels of Fig. 7). The computed decrease in shear stress in the middle layer (Fig. 6) is a result of the cross-shore pressure gradient, associated with the set-up of the mean water level, opposing the shear stress at the trough level. Within the bottom boundary layer, the wave-induced forcing, Eq. (14), becomes apparent, opposing the cross-shore pressure gradient (upper panels of Fig. 6). However, the total shear stress remains negative, resulting in an offshore directed flow within the bottom boundary layer, consistent with the observations. Note that the enhancement of the turbulent eddy viscosity within the

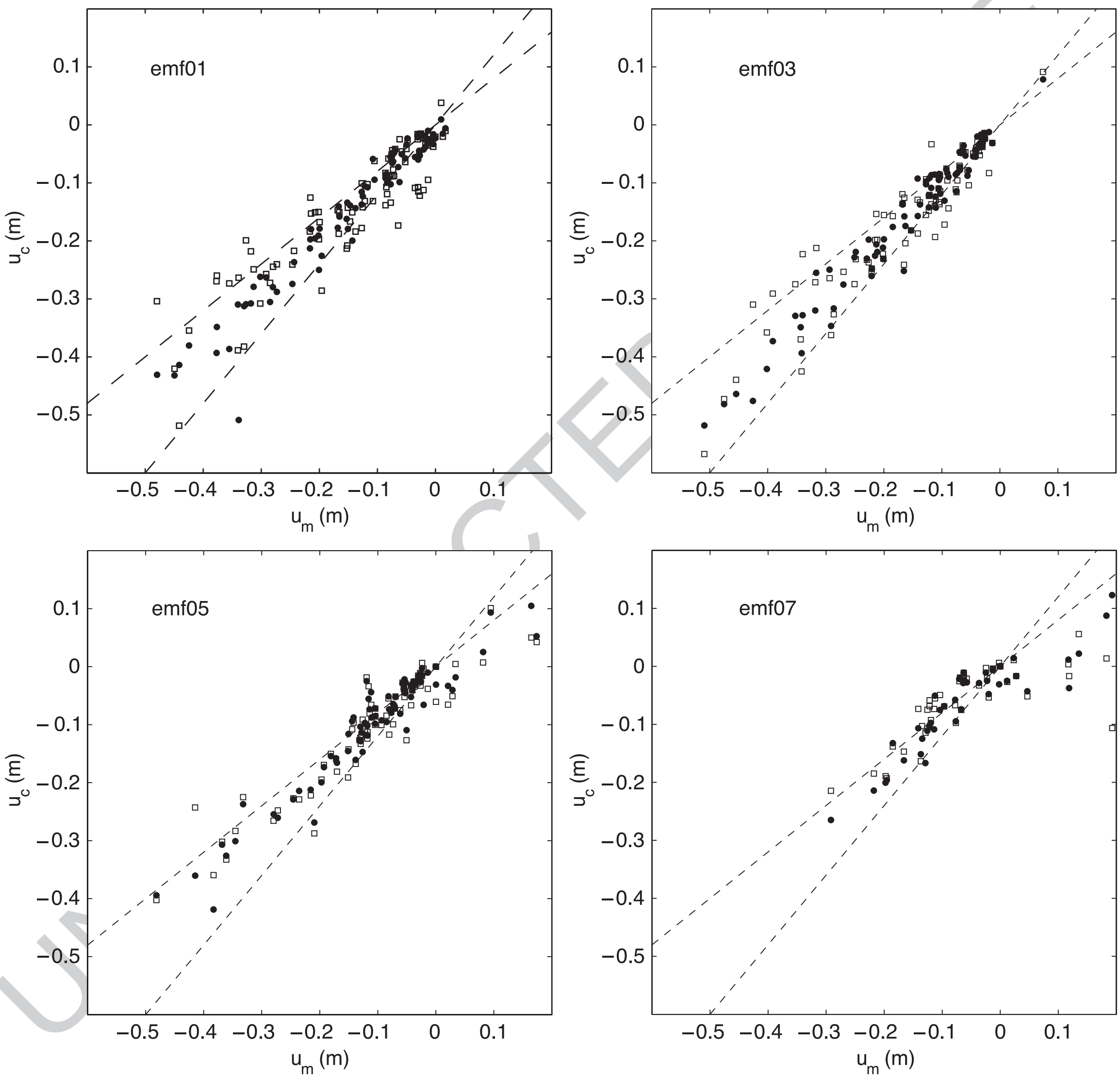

Fig. 9. Measurements compared with optimized predictions (dots) and calibrated predictions (squares) of the cross-shore flow velocities for all stations at four different positions within the vertical (see Table 2 for instrument elevation). Results only shown at times EMF is below trough level. Error bands (20%) given by the dashed lines.

bottom boundary layer, Eq. (20), is negligible compared to the wave-induced turbulence (upper panels of Fig. 7). The corresponding longshore current velocity distributions at the locations outside the surfzone (4 and 7) closely resemble a logarithmic profile (upper panels of Fig. 5), which is well represented by the optimized model results. The corresponding computed shear stress distributions (Fig. 6) show minimal vertical variation, indicating that the wave and wind-induced shear stresses at the surface are the main driving force for the longshore current at these locations outside the surfzone, i.e. no contributions from turbulent mixing, alongshore pressure gradients and shear instabilities.

For stations further inshore (locations 9 and 10), the effects of wave breaking become more prominent, with a strong curvature of the cross-shore flow near the surface in both measurements and computations (lower panels of Fig. 4) associated with the exertion of the roller-induced shear stress, which has increased significantly, O(10^2), compared with the stations outside the surfzone (compare upper and lower panels of Fig. 6). As a result the turbulent eddy viscosity has increased (lower panels of Fig. 7) and the maximum cross-shore flow velocity has shifted downward, again consistent with laboratory observations. The log-profile in both measurements and model computations is suppressed into a thin boundary layer. The measured longshore current profiles also exhibit this thin logarithmic layer, whereas the velocity profile in the middle layer is more depth-uniform (lower panels of Fig. 5). This deviation from the logarithmic distribution results in discrepancies between the measured and optimized computed velocity profiles. For the station closest to shore (10), additional forcing that is most likely related to lateral mixing is present (lower right panel of Fig. 8), resulting in a strong increase of the turbulent shear stress within the middle layer compared with the shear stress at the surface.

The predictive capability of the model is calculated using a skill measure for the two velocity components at each instrument, denoted by the subscript j, over the entire experiment (Gallagher et al., 1998):

$$\mathrm{skill}_j = 1 - \frac{\sqrt{<(u_{\mathrm{m},j} - u_{\mathrm{c},j})^2>}}{\sqrt{<(u_{\mathrm{m},j})^2>}} \tag{27}$$

where <> denotes ensemble averaging over all sled positions, the subscripts m and c refer to measured and computed velocities, respectively, and an equivalent expression is used for the alongshore velocities. The computed velocities are obtained utilizing optimized eddy viscosity and bottom friction at each station (i.e. minimizing Eq. (26)). The comparison of the measured and predicted cross-shore flow velocities at all sled stations for the lowest current meter, EMF01, at approximately 10 cm above the bed, shows predominantly offshore flow velocities (upper left panel of Fig. 9) with a skill of 0.85. The results for sensor EMF03, deployed at approximately 50 cm above the bed, also shows predominantly offshore directed flows, and a similar performance for the predicted flow conditions, with corresponding skill of 0.88 (upper right panel of Fig. 9). Examining a sensor higher in the water column, EMF05 at approximately 130 cm above the bed, shows both onshore and offshore directed velocities (lower left panel of Fig. 9). The onshore velocities are associated with the roller shear stress-driven cross-shore flow close to the

Table 2
Skill factors for cross-shore velocity for different scenarios

Scenario	EMF01	EMF02	EMF03	EMF04	EMF05	EMF06	EMF07	EMF08
Optimized PAR	0.85	0.84	0.88	0.85	0.66	0.49	0.74	0.64
Calibrated PAR	0.72	0.74	0.79	0.81	0.65	0.33	0.66	0.55
QW all days	0.54	0.55	0.55	0.46	0.35	0.35	0.38	0.25
QW day <290	0.68	0.67	0.69	0.61	0.52	0.11	0.32	0.10
Depth-averaged U	0.57	0.60	0.64	0.71	0.44	0.19	0.73	0.51
Optimized PWC	0.65	0.71	0.75	0.44	−0.37	−0.10	0.44	0.39

PAR corresponds to the parabolic eddy viscosity distribution, QW to the cases with computed cross-shore mass-flux, Eq. (28), as opposed to the inferred mass-flux, Eq. (23), and PWC to the piece-wise constant eddy viscosity distribution.

surface. The overall comparison is still favorable with a skill of 0.66. Even higher in the water column, EMF07 at approximately 220 cm above the bed, flow velocities are typically smaller than at the other sensors (lower right panel of Fig. 9), with a skill of 0.74. Skill measures for the cross-shore current predictions of all the EMF instruments are given in Table 2, showing a good correspondence between measurements and optimized computations.

The comparison between the measured and optimized predicted longshore current velocities is considered next. For the lowest sensor, EMF01, the predicted velocities are well within the 20% error bands (upper left panel of Fig. 10) with a corresponding skill

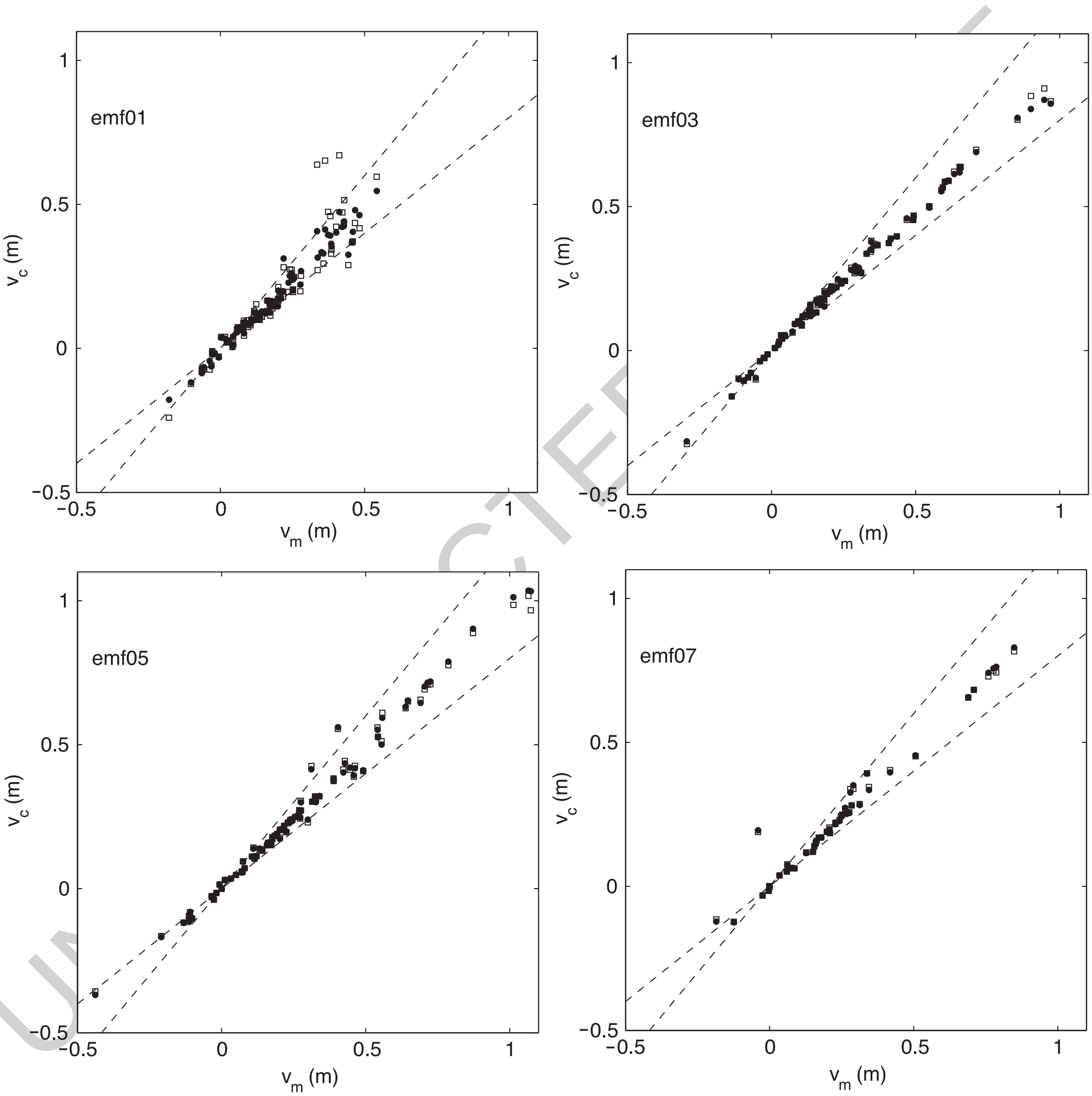

Fig. 10. Measurements compared with optimized predictions (dots) and calibrated predictions (squares) of the alongshore flow velocities for all stations at four different positions within the vertical (see Table 2 for instrument elevation). Results only shown at times EMF is below trough level. Error bands (20%) given by the dashed lines.

Table 3
Skill factors for alongshore-velocity for different scenarios

Scenario	EMF01	EMF02	EMF03	EMF04	EMF05	EMF06	EMF07	EMF08
Optimized PAR	0.87	0.88	0.93	0.95	0.94	0.95	0.97	0.95
Calibrated PAR	0.72	0.90	0.94	0.95	0.93	0.94	0.95	0.93
Depth-averaged V	0.40	0.87	0.92	0.93	0.89	0.90	0.88	0.86
Optimized PWC	0.82	0.90	0.92	0.92	0.89	0.87	0.84	0.78

PAR corresponds to the parabolic eddy viscosity distribution and PWC corresponds to the piece-wise constant eddy viscosity distribution.

of 0.87. At EMF03 the prediction of the alongshore velocities is improved with respect to EMF01 (upper right panel of Fig. 10) resulting in a skill of 0.93. Similar predictive capability is observed at sensors EMF05 and EMF07 with skill factors of 0.94 and 0.97, respectively. Skill measures for the alongshore current predictions of all the EMF instruments are given in Table 3, again showing a good correspondence between measurements and computations.

The results show that the model is capable of describing the observed vertical velocity distribution for both the cross-shore and alongshore flows utilizing a single description for the vertical turbulent eddy viscosity distribution. However, to be able to use the model in a more predictive mode, the eddy viscosity scale factor and bottom roughness should be known a priori. This requires a relationship for both the eddy viscosity and bottom roughness with some measurable physical quantities. Alternatively, if the model is not overly sensitive to the values of f_v and k_s, representative values could be used for all conditions.

The optimized eddy viscosity calibration factor (i.e. at each station), f_v, varies over a relatively small range, with most of the values between 0.02 and 0.2 (left panel of Fig. 11), which suggests a representative value may give reasonable predictions for the vertical distribution of the cross-shore and alongshore flows. It also suggests that the present parameterization of the eddy viscosity, i.e. with a dependence on wave breaking, wind and flow conditions (Eqs. (9), (10) and (11)) is adequate. The outliers, centered around $T=60$ h, correspond to offshore velocity profiles measured on day 291. It is likely that on day 291 the local wave conditions at these locations are subject to wave–current interaction due to the presence of a rip-channel (right panel of Fig. 2).

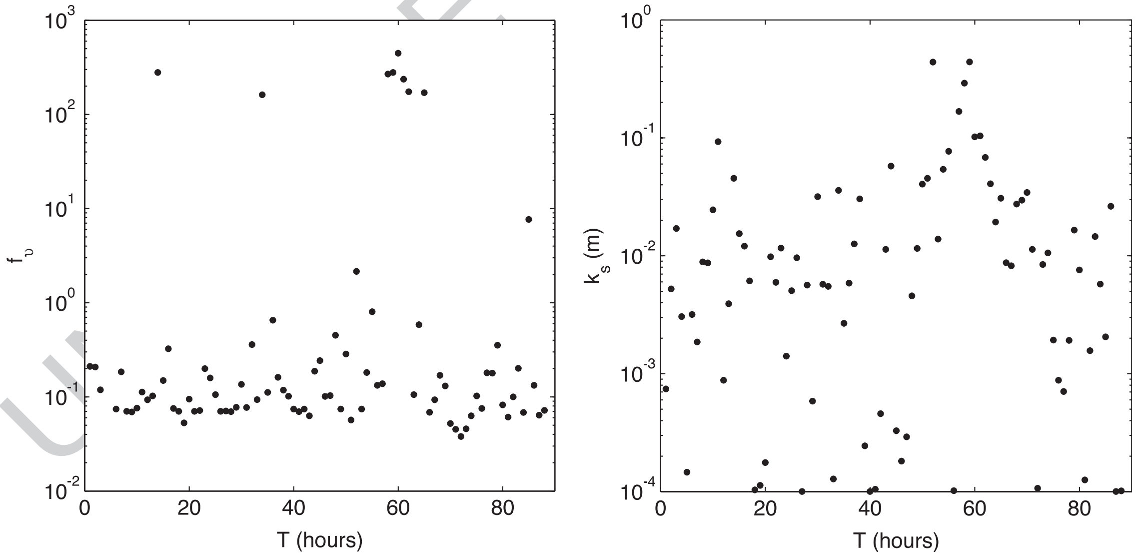

Fig. 11. Left panel: optimized values of f_v for each hour. Right panel: optimized values of the bottom roughness, k_s, for all hours.

The bottom roughness parameter varies considerably more (right panel of Fig. 11), with several orders of magnitude in differences between the various deployment positions of the sled. Utilizing the measured bathymetry profiles to relate the measured roughness to the optimal k_s showed no significant correlation for the present data set. Part of this can be explained by the fact that the model does not account for the increased roughness in the presence of waves (Grant and Madsen, 1979, Myrhaug and Slaattelid, 1989). Hence, the optimal k_s corresponds to an apparent bed roughness, k_a, and not the actual bed roughness.

The sensitivity of the model predictions to both f_v and k_s is examined next by computing the skill for the lowest (most critical) sensor for different combinations of f_v and k_s These computations show that for a f_v of O(0.1) the sensitivity to the bottom roughness is limited (Fig. 12). Only for large values of the bottom roughness, i.e. k_s>0.1, does the skill drop significantly. In view of the above, the optimal value of both the eddy viscosity scale factor, f_v = 0.101 m^2/s, and bottom roughness, k_s = 0.0082 m, are used in the calibrated predictions of the vertical distribution of the cross-shore and alongshore mean flows. Typical results of the calibrated model predictions are shown in Figs. 4 and 5. Overall, the differences between the optimized and calibrated model predictions are relatively small, with the largest differences occurring at the lowest sensor. This holds for both the cross-shore flow and the alongshore flow and is attributed to the fact that the velocity shear is significantly larger at this depth, i.e. bottom roughness plays an important role. This becomes apparent at station 7 where the optimal bottom roughness is two orders of magnitude smaller than the calibrated k_s (Table 4) and consequently the calibrated predictions underestimate the flow velocities near the bed (upper right panel of Figs. 4 and 5). At station 10, the opposite occurs, with a calibrated roughness that is significantly smaller than the optimal k_s (Table 4), resulting in an over-prediction of the near-bed flow velocity (lower right panel of Figs. 4 and 5). Still, the overall differences are relatively small, consistent with the sensitivity analysis.

The comparison of calibrated predictions with the measurements at all available stations and current

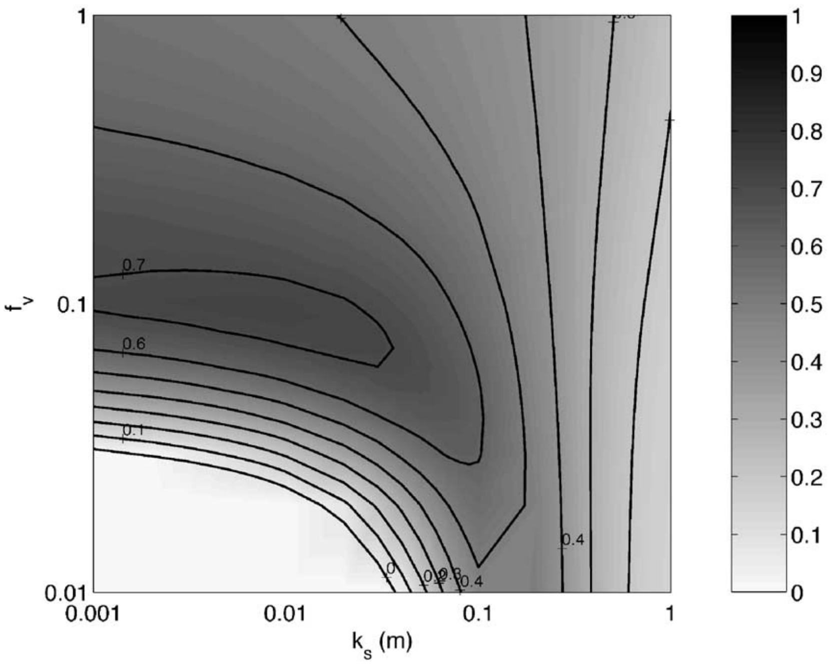

Fig. 12. Computed model skill for the cross-shore velocity at the EMF01 as function of f_v and k_s.

Table 4
Optimized f_v and k_s for yearday 288 at four sled positions (columns 3–4)

Station	X (m)	f_v	k_s	f_v	k_s
4	284.0	0.159	0.0014	0.101	0.0082
7	187.7	0.071	0.0001	0.101	0.0082
9	159.5	0.078	0.0006	0.101	0.0082
10	143.6	0.136	0.0317	0.101	0.0082

Calibrated f_v and k_s (columns 5–6, utilized for all stations).

meters shows an increased variability with respect to using the optimized values for the cross-shore velocities (Fig. 9), which is more profound for the lower sensors (upper panels of Fig. 9) than for the higher sensors (lower panels of Fig. 9). The corresponding skill at the various sensors has decreased by approximately 10–20% depending on their elevation (Table 2). The calibrated results for the longshore current only show increased variability for the lowest sensor (upper left panel of Fig. 10) with a corresponding decrease in skill of O(20) % to 0.72. The other sensors are not affected (Fig. 10 and Table 3). Considering the variability in wave conditions and bathymetry, the results indicate that the curvature of both the cross-shore and alongshore flows and the corresponding near-bed velocities can be predicted reasonably well with fixed values for f_v and k_s, provided the mass flux and the wave transformation are well predicted.

5. Discussion

The model predictions have been constrained by the mass flux inferred from the measured flow distribution, both in the cross-shore and alongshore directions (Eq. (23)). Generally this information will not be available a priori and a 1D or 2D model computation will be performed to compute the local depth-averaged velocities. This is examined in more detail in the following. In the case of alongshore uniformity, the depth-averaged cross-shore flow below the trough level, U_w, is assumed to compensate the wave-induced (Phillips, 1977) and roller-induced mass flux (Svendsen, 1984):

$$U_w = \frac{E_w k_x}{\rho \omega h_t} + \frac{2 E_r k_i}{\rho \omega h_t} \tag{28}$$

where E_w represents the wave energy and E_r represents the roller energy. Computing the roller energy, RB97 their Eq. (9) with the roller dissipation coefficient, $\beta = 0.05$ (Ruessink et al., 2001) and utilizing the estimated mass flux velocity, Eq. (28), instead of the inferred cross-shore mass flux velocity, Eq. (23), results in a significant degrading of the model skill (Table 2). Most of this decrease in skill can be explained by the fact that at times the bathymetry within the surfzone is far from alongshore uniform (see right panel of Fig. 2), and hence the onshore wave-induced mass flux is not necessarily locally compensated as undertow. Excluding the days of alongshore non-uniformity, i.e. excluding yeardays >289, results in a significant improvement (Table 2), with skill factors for the lower sensors comparable to the case with inferred mass flux. This suggests that the estimated mass flux and the corresponding mass flux velocity, U_w, are of the right order (Fig. 13), provided the bathymetry is alongshore uniform.

Velocity profile models are used in the modeling of the morphological evolution of cross-shore profiles (Roelvink and Broker, 1993). The main objective of utilizing the vertical flow models is to predict the near-bed flow velocities to drive the sediment transport. Taking into account the power

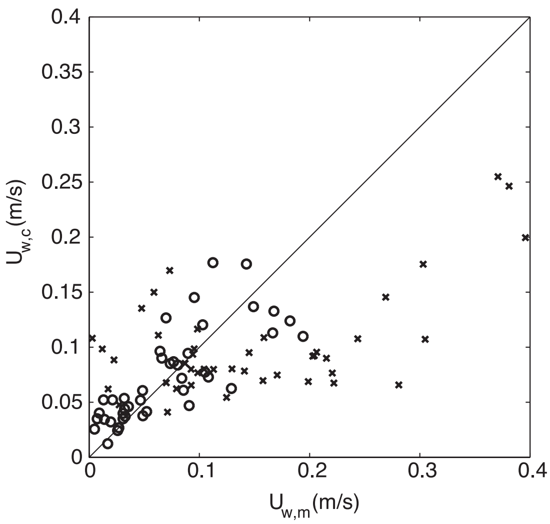

Fig. 13. Comparison of measured and estimated mass-flux velocity utilizing $\beta = 0.05$ for calibrated predictions and yeardays ≤ 289 (circles) and yeardays >290 (crosses).

law associated with sediment transport (e.g. Bailard, 1981):

$$S \sim u_{\mathrm{b}}^{p} \tag{29}$$

where S is the sediment transport rate, u_{b} represents the velocity close to the bed and p equals 3 or 4, emphasizes the importance of an accurate prediction of the near-bed velocities. The difference between the velocity near the bed and the depth-averaged flow is a function of the vertical curvature, and it is assumed that the vertical flow models have an improved skill in predicting the near-bed velocity compared with depth-averaged flow models. This is demonstrated by utilizing the depth-averaged flow velocity as a predictor for velocities at the various current meters. This results in a significant loss of skill, O(20%) for the cross-shore flow and O(40%) for the alongshore flow, compared with the calibrated case, for the lowest current meter (Tables 2 and 3). This suggests that the application of the velocity profile model in the modeling of sediment dynamics is warranted.

The vertical distribution of the eddy viscosity plays an important role in the resulting velocity profiles. This is demonstrated by computing the velocity distribution for a piece-wise constant eddy viscosity distribution, frequently used for the computation of the return flow structure (e.g. Svendsen and Lorenz, 1989). Again optimizing for both f_v and k_s results in model skills that are generally lower than for the parabolic distribution for both the cross-shore velocity (Table 2) and the alongshore velocity (Table 3). This suggests that if a single description of the vertical distribution of the turbulent eddy viscosity is used in modeling both the cross-shore and alongshore flow structure, a parabolic distribution is better than a piece-wise-constant eddy viscosity distribution.

6. Conclusions

Observations of the vertical structure of the mean flow during the Sandy Duck field experiment have been presented. Strong cross-shore flow velocities were observed in the lower part of the water column under wave-breaking conditions. For non-breaking conditions, maximum flow velocities occur generally in the upper part of the water column. Both of these observations are consistent with observations obtained during earlier laboratory experiments. The measured longshore current velocity profiles are logarithmic under non-breaking conditions and become more depth-uniform under breaking conditions, in line with previous observations.

An existing model formulation has been used in the comparison with observations. The model is capable of describing the vertical structure of the mean flow, provided the wave transformation and the associated mass flux are modeled correctly and a parabolic distribution for the eddy viscosity is used. If a single piece-wise constant eddy viscosity distribution is used, the overall model skill drops. Utilizing calibrated values by optimizing over the entire experiment the eddy viscosity scale factor, f_v, and the bottom roughness, k_s, results in a model skill of O(70) % for the lower sensors. Utilizing the estimated mass flux gives a slightly lower performance, provided the bathymetry is alongshore uniform, which suggests the mass flux is well predicted by the wave transformation model. It is concluded that the application of the velocity profile model within a depth-averaged flow model, driven by a wave transformation model that includes surface rollers, is expected to result in an improved description of the near-bed velocities, which is important for sediment transport processes.

Acknowledgements

We thank Enrico Foti, Frank Wiersma, Rob Wyland, Mark Orzech and Edie Gallager for their collaboration in collecting the measurement data during Sandy Duck. Additional data were provided by the Field Research Facility of the U.S. Army Engineer Waterways Experiment Station's Coastal Engineering Research Center. Permission to use these data is appreciated. EBT and TS were funded by the Office of Naval Research, Coastal Science Program, under contract N00014-01-WR-20023. Part of the work presented in this paper was done while AR held a National Research Council-NPS Research Associateship. Additional funding for AR was provided by the Dutch National Science Foundation (NWO) contract DCB.5856. We thank the reviewers for their constructive comments.

Appendix A. Vertical distribution of eddy viscosity

The vertical distribution of the turbulent eddy viscosity is written as a product of a shape factor, ϕ_s, and a parabolic shape function:

$$\nu_t = \phi_s \bar{\nu}_t \sigma(\sigma_s - \sigma) \quad \text{(A1)}$$

where σ_s represents the upper limit at which the eddy viscosity is zero (Fig. A1) and $\bar{\nu}_t$ depends on the individual contributions of wave-, wind- and flow-induced turbulence (Eq. (12)). The shape factor, ϕ_s, follows from the condition that the depth-integrated

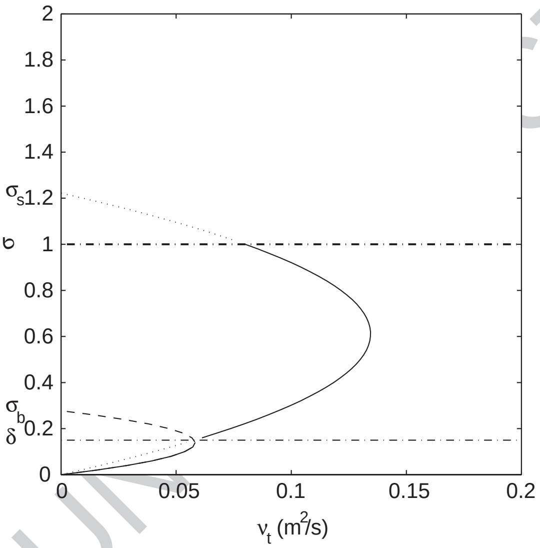

Fig. A1. Example of a vertical distribution of turbulent eddy viscosity (solid line) with corresponding σ-parameters. Trough level (thick dash-dotted line) and wave boundary layer (thin dash-dotted line) given as a reference. Dotted lines complete the distribution according to Eq. (A1) and the dashed line completes the distribution according to Eq. (A6).

vertically varying eddy viscosity should equal the depth-averaged eddy viscosity, hence:

$$\int_o^1 \phi_s \sigma(\sigma_s - \sigma) d\sigma = 1 \quad \text{(A2)}$$

which yields:

$$\phi_s = \frac{1}{\frac{1}{2}\sigma_s - \frac{1}{3}} \quad \text{(A3)}$$

The value of σ_s depends on the relative magnitude of the various turbulence contributions (Eq. (12)). In the presence of wave breaking and wind, turbulence is injected into the upper layer of the flow. This process is simulated with an increased eddy viscosity at the surface, $\nu_{t,\mathrm{surface}}$. Combining Eq. (A1) at the surface, i.e. $\sigma = 1$, and Eq. (A3) gives:

$$\sigma_s = \frac{\bar{\nu}_t - \frac{1}{3}\nu_{t,\mathrm{surface}}}{\bar{\nu}_t - \frac{1}{2}\nu_{t,\mathrm{surface}}} \quad \text{(A4)}$$

The eddy viscosity at the surface is defined as:

$$\nu_{t,\mathrm{surface}} = \frac{3}{2}\sqrt{\bar{\nu}^2_{t,\mathrm{wind}} + \bar{\nu}^2_{t,\mathrm{wave}})} \quad \text{(A5)}$$

which in the absence of flow induced turbulence results in a σ_s of 2 (viz. Eq. (A4)), i.e. the maximum eddy viscosity is located at the surface level. In the absence of wave breaking and wind σ_s equals 1, corresponding to a situation where there is no input of turbulent kinetic energy at the surface. In the case of combined eddy viscosity contributions, σ_s ranges between 1 and 2.

The vertical distribution of the eddy viscosity in the bottom boundary layer is obtained by including additional friction-induced eddy viscosity (Eq. (21)), and is again described as product of a scale factor and a parabolic shape function (Fig. A1):

$$\nu_t = (\phi_s \bar{\nu}_t + \phi_b \bar{\nu}_{tb})(\sigma_b - \sigma)\sigma \quad \text{(A6)}$$

where the value of σ_b depends on the relative magnitude of the additional eddy viscosity in the bottom boundary layer and the eddy viscosity distribution in the middle layer:

$$\sigma_{\mathrm{b}} = \frac{\phi_{\mathrm{s}}\bar{v}_{\mathrm{t}}\sigma_{\mathrm{s}} + \phi_{\mathrm{b}}\bar{v}_{\mathrm{tb}}\delta}{\phi_{\mathrm{s}}\bar{v}_{\mathrm{t}} + \phi_{\mathrm{b}}\bar{v}_{\mathrm{tb}}} \tag{A7}$$

The shape factor for the bottom boundary layer follows from the constraint:

$$\frac{1}{\delta}\int_{o}^{\delta} \phi_{\mathrm{b}}\sigma(\delta-\sigma)d\sigma = 1 \tag{A8}$$

which yields:

$$\phi_{\mathrm{b}} = \frac{6}{\delta^2} \tag{A9}$$

Appendix B. Vertical distribution of mean flow velocity

In the following, the analytical expressions describing the vertical distribution of the flow velocity within the middle layer and boundary layer are presented. Starting with the velocity gradient within the middle layer given by:

$$\frac{\partial u_i}{\partial \sigma} = \frac{h_{\mathrm{t}}}{\rho\phi_{\mathrm{s}}\bar{v}_{\mathrm{t}}}\left(\frac{(\tau_{\mathrm{t},i} - F_i) + F_i\sigma}{\sigma(\sigma_{\mathrm{s}} - \sigma)}\right) \tag{B1}$$

which is rewritten to facilitate the vertical integration:

$$\frac{\partial u_i}{\partial \sigma} = A\left(\frac{B_i}{\sigma_{\mathrm{s}}\sigma} + \frac{\frac{B_i}{\sigma_{\mathrm{s}}} + C_i}{\sigma_{\mathrm{s}} - \sigma}\right) \tag{B2}$$

where the coefficients are given by:

$$A = \frac{h_{\mathrm{t}}}{\rho\phi_{\mathrm{s}}\bar{v}_{\mathrm{t}}} \tag{B3}$$

$$B_i = \tau_{\mathrm{t},i} - F_i \tag{B4}$$

$$C_i = F_i \tag{B5}$$

The vertical distribution of the velocity in the middle layer is obtained by the integration of Eq. (B2), subject to the condition that the velocity at the bottom of the middle layer matches the velocity at the top of the bottom boundary layer, $u_{\delta,i}$:

$$u_i = u_{\delta,i} + A\left(\frac{B_i}{\sigma_{\mathrm{s}}}\ln\frac{\sigma}{\delta} - \left(\frac{B_i}{\sigma_{\mathrm{s}}} + C_i\right)\ln\frac{\sigma_{\mathrm{s}} - \sigma}{\sigma_{\mathrm{s}} - \delta}\right) \tag{B6}$$

A similar procedure is followed for the bottom boundary layer, where the velocity gradient is given by:

$$\frac{\partial u_i}{\partial \sigma} = \frac{h_{\mathrm{t}}}{\rho(\phi_{\mathrm{s}}\bar{v}_{\mathrm{t}} + \phi_{\mathrm{b}}\bar{v}_{\mathrm{tb}})} \times \left(\frac{(\tau_{\mathrm{t},i} - F_i + \frac{D_{\mathrm{f}}k_i}{\omega}) + (F_i - \frac{D_{\mathrm{f}}k_i}{\delta\omega})\sigma}{\sigma(\sigma_{\mathrm{b}} - \sigma)}\right) \tag{B7}$$

which is written as:

$$\frac{\partial u_i}{\partial \sigma} = A_{\mathrm{b}}\left(\frac{B_{\mathrm{b},i}}{\sigma_{\mathrm{b}}\sigma} + \frac{\frac{B_{\mathrm{b},i}}{\sigma_{\mathrm{b}}} + C_{\mathrm{b},i}}{\sigma_{\mathrm{b}} - \sigma}\right) \tag{B8}$$

where the coefficients are given by:

$$A_{\mathrm{b}} = \frac{h_{\mathrm{t}}}{f_v\rho\phi_{\mathrm{s}}\bar{v}_t + \rho\phi_{\mathrm{b}}\bar{v}_{\mathrm{tb}}} \tag{B9}$$

$$B_{\mathrm{b},i} = (\tau_{\mathrm{t},i} - F_i + \frac{D_{\mathrm{f}}k_i}{\omega}) \tag{B10}$$

$$C_{\mathrm{b},i} = \left(F_i - \frac{D_{\mathrm{f}}k_i}{\delta\omega}\right) \tag{B11}$$

Integration of Eq. (B8), subject to the boundary condition that $u_i = 0$ at $\sigma = \sigma_0$, yields:

$$u_i = A_{\mathrm{b}}\left(\frac{B_{\mathrm{b},i}}{\sigma_{\mathrm{b}}}\ln\frac{\sigma}{\sigma_0} - \left(\frac{B_{\mathrm{b},i}}{\sigma_{\mathrm{b}}} + C_{\mathrm{b},i}\right)\ln\frac{\sigma_{\mathrm{b}} - \sigma}{\sigma_{\mathrm{b}} - \sigma_0}\right) \tag{B12}$$

This equation is valid for $\sigma > e\sigma_0$. A linear velocity decay towards the bottom is used below this level. The depth-integrated velocity is obtained by integrating Eqs. (B6) and (B12) over the middle layer and bottom boundary layer, respectively.

References

Arcilla, A.S., Roelvink, J.A., O'Connor, B.A., Reniers, A., Jimenez, J.A., 1994. The Delta flume '93 experiment. Proceedings Coastal Dynamics '94. ASCE, pp. 488–502.

Bailard, J.A., 1981. An energetic total load sediment transport model for a plane sloping beach. J. Geophys. Res. 86, 10938–10954.

Battjes, J.A., 1975. Modelling of turbulence in the surfzone. Proceedings Symposium on Modeling Techniques, 1050–1061.

Battjes, J.A., Janssen, J.P.F.M., 1978. Calibration and verification of a dissipation model for random breaking waves. Proceedings of the 16th International Conference on Coastal Engineering. ASCE, pp. 569–587.

Bowen, A.J., Holman, R.A., 1989. Shear instabilities of the mean longshore current: 1. Theory. J. Geophys. Res. 94, 18023–18030.

Church, C.C., Thornton, E.B., 1993. Effects of wave-breaking induced turbulence within a longshore current model. Coast. Eng. 20, 1–28.

Dally, W., 1980. A numerical model for beach profile evolution, Master's thesis. University of Delaware, Newark.

Davies, A.M., 1988. On formulating two-dimensional vertically integrated hydrodynamic numerical models with an enhanced representation of bed stress. J. Geophys. Res. 93, 1241–1263.

Deigaard, R., 1993. A note on the three dimensional shear stress distribution in a surf zone. Coast. Eng. 20, 157–171.

de Vriend, H.J., Stive, M.J.F., 1987. Quasi-3D modelling of nearshore currents. Coast. Eng. 11, 565–601.

Dingemans, M.W., Radder, A.C., de Vriend, H.J., 1987. Computation of the driving forces of wave-induced currents. Coast. Eng. 11, 539–563.

Dong, P., Anatasiou, K., 1991. A numerical model of the vertical distribution of longshore currents on a plane beach. Coast. Eng. 15, 279–298.

Dyhr-Nielsen, M., Sorensen, T., 1970. Some sand transport phenomena on coasts with bars. Proceedings of the 12th International Conference on Coastal Engineering. ASCE, pp. 855–866.

Fredsoe, J., Deigaard, R., 1992. Mechanics of Coastal Sediment Transport. World Scientific, Singapore.

Gallagher, E.L., Elgar, S., Guza, R.T., 1998. Observations of sand bar evolution on a natural beach. J. Geophys. Res. 103, 3203–3215.

Gallagher, E.L., Thornton, E.B., Stanton, T.P., 2003. Sand bed roughness in the nearshore. J. Geophys., 108 (doi:10.1029/2001JC001081).

Garcez Faria, A.F., Thornton, E.B., Stanton, T.P., Soares, C.V., Lippmann, T.C., 1998. Vertical profiles of longshore currents and related bed shear stress and bottom roughness. J. Geophys. Res. 103, 3217–3232.

Garcez Faria, A.F., Thornton, E.B., Lippmann, T.C., Stanton, T.P., 2000. Undertow over a barred beach. J. Geophys. Res. 105, 16999–17010.

Grant, W.D., Madsen, O.S., 1979. Combined wave and current interaction with a rough bottom. J. Geophys. Res. 84, 1797–1908.

Haines, J.W., Sallenger Jr., A.H., 1994. Vertical structure of mean cross-shore currents across a barred surfzone. J. Geophys. Res. 99, 14223–14242.

Hamilton, D.G., Ebersole, B.A., 2001. Establishing uniform longshore currents in a large-scale sediment transport facility. Coast. Eng. 42, 199–218.

Hansen, J.B., Svendsen, I.A., 1984. A theoretical and experimental study of undertow. Proceedings of the 19th International Conference on Coastal Engineering. ASCE, pp. 2246–2262.

Jonsson, I.G., 1966. Wave boundary layers and friction factors. Proceedings of the 10th International Conference on Coastal Engineering. ASCE, pp. 127–148.

Klopman, G., 1994. Vertical structure of the flow due to waves and current. WL-Delft Hydraulics report H840.30. Part II.

Long, C.E., Atmadja, J., 1994. Index and bulk parameters for frequency-directional spectra measured at CERC Field Research Facility, September 1990 to August 1991, Miscellaneous paper CERC-94-5, U.S. Army Waterways Experiment Station, Vicksburg, MS.

Longuet-Higgins, M.S., 1953. Mass transport in water waves. Philos. Trans. R. Soc. Lond., A, 535–581.

Myrhaug, D., Slaattelid, O., 1989. Combined wave and current boundary layer model for fixed rough seabeds. Ocean Eng. 16, 119–142.

Nadaoka, K., Kondoh, T., 1982. Laboratory measurements of velocity field structure in the surfzone by LDV. Coast. Eng. Jpn. 25, 125–145.

Okayasu, A., Shibayama, T., Horikawa, K., 1988. Vertical variation of undertow in the surfzone. Proceedings of the 21st International Conference on Coastal Engineering, pp. 478–491.

Ozkan-Haller, H.T., Kirby, J.T., 1999. Non-linear evolution of shear instabilities of the longshore current: a comparison of observations and computations. J. Geophys. Res. 104, 25953–25984.

Phillips, O.M., 1977. The Dynamics of the Upper Ocean, 2nd ed. Cambridge Univ. Press, New York. 336 pp.

Putrevu, U.J., Svendsen, I.A., 1993. Vertical structure of undertow outside the surf zone. J. Geophys. Res. 98, 12707–12716.

Putrevu, U.J., Oltman-Shay, J., Svendsen, I.A., 1995. Effect of alongshore non-uniformities on longshore current predictions. J. Geophys. Res. 100, 16119–16130.

Reniers, A.J.H.M., Battjes, J.A., 1997. A laboratory study of longshore currents over barred and non-barred beaches. Coast. Eng. 30, 1–22.

Reniers, A.J.H.M., Thornton, E.B., Lippmann, T.C., 1995. Longshore currents over barred beaches. Proc. of the Coastal Dynamics Conference '95. ASCE, pp. 413–424.

Roelvink, J.A., Broker, I., 1993. Cross-shore profile models. Coast. Eng. 21, 193–224.

Roelvink, J.A., Reniers, A.J.H.M., 1994. Upgrading of a quasi-3D hydrodynamic model, Abstracts-in-depth, MAST G8-M overall workshop, Gregynog.

Ruessink, B.G., Miles, J.R., Feddersen, F., Guza, R.T., Elgar, S., 2001. Modeling the alongshore current on barred beaches. J. Geophys. Res. 106, 22451–22463.

Simons, R.R., Grass, T.J., Mansour-Tehrani, M., 1992. Bottom shear stresses in the boundary layers under waves and currents crossing at right angles. Proceedings of the 23rd International Conference on Coastal Engineering. ASCE, pp. 604–617.

Smith, J.M., Svendsen, I.A., Putrevu, U., 1992. Vertical structure of the nearshore current at Delilah: measured and modeled. Proceedings of the 23rd International Conference on Coastal Engineering. ASCE, pp. 2825–2838.

Soulsby, R.L., 1997. Dynamics of Marine Sands. Thomas Telford, London.

Stive, M.J.F., Wind, H.G., 1986. Cross-shore mean flow in the surf zone. Coast. Eng. 10, 325–340.

Svendsen, I.A., 1984. Mass flux and undertow in a surf zone. Coast. Eng. 8, 347–365.

Svendsen, I.A., Buhr Hansen, J., 1988. Cross-shore currents in surf-zone modelling. Coast. Eng. 12, 23–42.

Svendsen, I.A., Lorenz, R.S., 1989. Velocities in combined undertow and longshore currents. Coast. Eng. 13, 55–79.

Svendsen, I.A., Schaffer, H.A., Buhr Hansen, J., 1987. The interaction between undertow and the boundary layer flow. J. Geophys. Res. 92, 11845–11856.

Thornton, E.B., Guza, R.T., 1986. Surf-zone longshore currents and random waves: field data and models. J. Phys. Oceanogr. 16, 1165–1178.

Thornton, E.B., Swayne, J.L., Dingler, J.R., 1998. Small-scale morphology across the surf zone. Mar. Geol. 145, 173–196.

Ting, F.C.K., Kirby, J.T., 1994. Observations of undertow and turbulence in a laboratory surfzone. Coast. Eng. 24, 51–80.

Van Dongeren, A.R., Svendsen, I.A., 2000. Nonlinear 3D effects in leaky infragravity waves. Coast. Eng. 41, 467–496.

Visser, P.J., 1984. Uniform longshore current measurements and calculations. Proc. 19th Int. Conf. Coastal Eng.. ASCE, pp. 11845–11856.

Whitford, D.J., Thornton, E.B., 1993. Comparison of wind and wave forcing of longshore currents. Cont. Shelf Res. 103, 1205–1218.